JOURNAL OF GEOPHYSICAL RESEARCH, VOL. 107, NO. A8, 1179, 10.1029/2001JA000219, 2002

A model of the near magnetosphere with a dawn-dusk asymmetry
1. Mathematical structure

N. A. Tsyganenko

Universities Space Research Association and Laboratory for Extraterrestrial Physics, NASA Goddard Space Flight Center, Greenbelt, Maryland, USA

Received 20 July 2001; revised 27 September 2001; accepted 28 September 2001; published 13 August 2002.

[1] A new empirical magnetic field model has been developed, representing the variable configuration of the inner and near magnetosphere for different interplanetary conditions and the ground disturbance levels. This paper describes the mathematical structure of the model, while the results of fitting it to a new set of spacecraft data are presented in a companion paper. The general approach remains the same as in the earlier T96 model, but the mathematical description of all major sources of the magnetospheric field now applies recently developed new methods. In particular, the field deformation technique is extensively used, making it possible to realistically and flexibly represent the fields of the cross-tail current, the ring current, and the Region 1 and 2 Birkeland currents. The new model ring current includes not only the axisymmetric component but also a partial ring current with field-aligned closure currents, a feature absent in earlier data-based models. The field of the cross-tail current includes two modules whose current densities vary along the Sun-Earth line with different rates. The cross-tail current sheet warps in two dimensions in response to the geodipole tilt, its inner edge shifts along the Sun-Earth line with growing disturbance, and its thickness varies along and across the tail. Birkeland currents of Regions 1 and 2 vary in response to interplanetary conditions, so that at ionospheric altitudes they shift in latitude and change their distribution in local time. The magnetospheric boundary is specified using a most recent empirical model [*Shue et al.*, 1998]; its size is controlled by the solar wind ram pressure, and its shape also varies in response to changes of the Earth's dipole tilt angle. The model magnetopause ensures a full confinement of the fields of all sources inside the magnetopause, regardless of its shape and size. The model also includes an interplanetary magnetic field–controlled interconnection field, allowing a finite normal B_n at the magnetopause and hence open magnetospheric configurations. *INDEX TERMS:* 2708 Magnetospheric Physics: Current systems (2409); 2730 Magnetospheric Physics: Magnetosphere—inner; 2740 Magnetospheric Physics: Magnetospheric configuration and dynamics; 2753 Magnetospheric Physics: Numerical modeling; 2778 Magnetospheric Physics: Ring current; *KEYWORDS:* inner magnetosphere, geomagnetic field models, partial ring current, field-aligned currents, magnetopause

1. Introduction

[2] The data-based approach to the modeling of the geomagnetosphere has been developed over the last 3 decades, starting with the pioneering work by *Mead and Fairfield* [1975]. Subsequent efforts [*Tsyganenko and Usmanov*, 1982; *Tsyganenko*, 1987, 1989] resulted in more refined models, useful in many studies. The principal goal of data-based magnetosphere modeling is to extract full information from large sets of available data, bridge the gap between theory and observations, and help answer a fundamental question "What is the actual structure of the geospace magnetic field and how is it related to changing interplanetary conditions and the ground disturbance level?"

[3] The recent rapid growth in the use of data-based models and the ever-growing demand for more flexible and more accurate ones were matched by substantial progress in their development. A new T96 model [*Tsyganenko*, 1995, 1996] was developed with continuous dependence on the solar wind pressure, interplanetary magnetic field (IMF), and Dst index, replacing earlier binning into several *Kp* index intervals. Another important improvement in that model was the introduction of an explicitly defined magnetopause, with realistic shape and with its size controlled by the solar wind, in contrast with earlier models which did not specify the boundary explicitly but used an uncontrolled defacto magnetopause. In addition, the interconnection of the geomagnetic field with the IMF across the magnetopause

0148-0227/02/2001JA000219$09.00

was included in the model, producing open magnetospheric configurations. The model also included for the first time the magnetic field of the Region 1 and 2 Birkeland currents, by using the approach of *Tsyganenko and Stern* [1996].

[4] However, all these improvements notwithstanding, the T96 model still contained serious shortcomings. In particular, because of an oversimplified approximation for the ring current, the model field in the inner magnetosphere was found generally overstretched [*Tsyganenko*, 2001; *Ganushkina et al.*, 2001], especially during strongly disturbed conditions. Another long-standing deficiency of the data-based models was their inability to replicate the strong dawn-dusk asymmetry of the inner magnetosphere during stormy periods.

[5] The purpose of this work is to present a new model, based on a completely revised mathematical framework, a new set of spacecraft data, and an improved method of parameterizing the external field sources by the solar wind state variables. In this article a detailed description is given of the elements of the new model, while its fitting to space magnetometer data is presented in the companion paper [*Tsyganenko*, 2002], hereinafter called Paper 2.

2. Overview of the Model's Structure

[6] The magnetic field within the modeling region is represented in modular fashion, regarding the external part of the total field $\mathbf{B}_\mathrm{E}$ (that is, without the Earth's main field) as the sum of contributions from major magnetospheric magnetic field sources

$$\mathbf{B}_\mathrm{E} = \mathbf{B}_\mathrm{CF} + \mathbf{B}_\mathrm{RC} + \mathbf{B}_\mathrm{T} + \mathbf{B}_\mathrm{FAC} + \mathbf{B}_\mathrm{INT}, \tag{1}$$

where $\mathbf{B}_\mathrm{CF}$ is the field of the Chapman-Ferraro currents which confine the Earth's main field inside the model boundary. The next three terms, $\mathbf{B}_\mathrm{RC}$, $\mathbf{B}_\mathrm{T}$, and $\mathbf{B}_\mathrm{FAC}$, are the contributions of the ring current, cross-tail current sheet, and large-scale field-aligned currents, respectively. Each of these terms includes a corresponding shielding field, to ensure a full confinement of the total magnetic field inside the model magnetopause. The last term in equation (1), $\mathbf{B}_\mathrm{INT}$, represents a partial penetration of the IMF inside the model magnetosphere. That term is a potential magnetic field, fully defined by a distribution of its normal component on the model boundary, which is found to depend on the strength and orientation of the IMF. It should be stressed that while the mathematical framework is made to fit the observed current patterns, all its parameters are derived from observations.

[7] In general, the above structure of the external field is similar to the one assumed in the T96 model. However, here individual terms in equation (1) are given by largely different mathematical forms. In particular, the ring current and Birkeland current field models have been replaced by more realistic and flexible approximations, as described in sections 2.1 and 2.3, respectively.

2.1. Model Ring Current

[8] One of the main goals of this effort was to improve the modeling of the inner magnetic field. To that end, a new model was devised for the ring current, a principal source of the observed external **B** in the region $R < 8R_E$. Instead of simple empirical ring currents, used in the T96 and earlier works [*Tsyganenko and Usmanov*, 1982; *Tsyganenko*, 1987, 1989], a more sophisticated and accurate approximation has been used here, based on the electric current calculated from an observed distribution of the particle pressure and anisotropy. It also takes into account the strong dawn-dusk asymmetry of the ring current during disturbed times, a feature neglected in all previous data-based models. A detailed description of the asymmetric model ring current is given elsewhere [*Tsyganenko*, 2000], and readers are referred to it for specific details of derivation and structure.

[9] Here we concentrate on further modifications, aimed at replicating basic effects of magnetic storms. The original model consisted of two modules: the first module represented the axially symmetric part of the ring current (SRC), and the second one represented the partial ring current (PRC), including field-aligned currents associated with the local time asymmetry of the azimuthal current. In the original model the SRC was based on quiet time profiles of the pressure and anisotropy, obtained earlier by *Lui and Hamilton* [1992], and in principle, the same method could have been used for the modeling of the storm time field in the inner magnetosphere. However, lack of data on the global storm time particle distribution, its variability, and complexity made it hard to devise a reasonably simple and flexible model.

[10] For that reason, the approach pursued here is a compromise. In essence, it singles out and reproduces only the following most important storm time effects: (1) an increase of the total magnitude of the ring current, which roughly tracks the variation of the corrected *Dst* index, (2) the penetration of energetic particles deep into the inner magnetosphere, convincingly demonstrated by numerical simulations [e.g., *Fok et al.*, 1996, 1999; *Kozyra et al.*, 1998], and requiring a variable characteristic size of the model ring current (the T96 model ring current had a fixed radius), and (3) a dramatic buildup of the asymmetric PRC, resulting in much larger plasma pressure and more depressed magnetic field in the evening sector [e.g., *Liemohn et al.*, 2001], and hence strong field-aligned currents, diverting the excess of the azimuthal current from the duskside.

[11] The above effects can be reproduced by a relatively simple modification of the original ring current model. The overall magnitudes of the SRC and PRC can be gauged by the corrected *Dst* index (or by its predicted value), and their spatial dimensions can be uniformly scaled by introducing factors ξ_S and ξ_P, so that $\mathbf{B}'_\mathrm{SRC}(\mathbf{r}) = \mathbf{B}_\mathrm{SRC}(\mathbf{r}/\xi_\mathrm{S})$, $\mathbf{B}'_\mathrm{PRC}(\mathbf{r}) = \mathbf{B}_\mathrm{PRC}(\mathbf{r}/\xi_\mathrm{P})$. In addition, to model a development of the duskside depression at the main phase of a storm, the PRC can be rotated toward the duskside by an angle δ, depending on the storm's intensity and phase. More details on the model parameterization are given in Paper 2.

[12] The fields of the symmetrical and partial components of the ring current must also be kept confined within the model magnetopause, for any values of the solar wind pressure, dipole tilt angle, the scaling factors, and the rotation angle. That question will be addressed in detail in section 2.4.2.2.

2.2. Modeling the Field of the Cross-Tail Current

[13] The magnetotail field model is based on principles and methods, developed in our earlier works [*Tsyganenko and Peredo*, 1994; *Tsyganenko*, 1995, 1998]. The model tail

Table 1. Parameters of the Cross-Tail Current Sheet, Entering in Equations (2), (3), (4), and (5)

i	f_i	b_i	c_i
1	−71.093466	10.901012	0.79540700
2	−1014.3086	12.683939	0.67166018
3	−1272.9394	13.517920	1.17486632
4	−3224.9359	14.867750	2.56524992
5	−44546.862	15.123064	10.0198679

field consists of independent "modules," that is, fields produced by current sheets with different rates of outward decrease of the current density, and the share of each "partial" field is adjusted to fit the data best. Each module is provided with its own shielding field (similar to $\mathbf{B}_{\mathrm{CF}}$) so that the total tail field always remains confined within the magnetopause. More discussion of the tail shielding field is given in section 2.4.2.1.

2.2.1. Initial model (no dipole tilt)

[14] The field of the cross-tail current sheet is given by the vector potential $\mathbf{A} = A_\varphi \mathbf{e}_\phi$ with

$$A_\phi = \rho \sum_{i=1}^{N} f_i \frac{t_i\sqrt{1-t_i^2}}{S_i^{(1)} S_i^{(2)}}, \tag{2}$$

where {ρ, φ, Z} form a cylindrical coordinate system, coaxial with the Z_{GSM} axis. The quantities t_i, $S_i^{(1)}$, and $S_i^{(2)}$ are defined as

$$t_i = \frac{2b_i}{S_i^{(1)} S_i^{(2)}}, \tag{3}$$

$$S_i^{(1)} = \sqrt{(\rho + b_i)^2 + (\zeta + c_i)^2}, \tag{4}$$

$$S_i^{(2)} = \sqrt{(\rho - b_i)^2 + (\zeta + c_i)^2}, \tag{5}$$

where $\zeta = \sqrt{Z^2 + D^2}$. Equations (2), (3), (4), and (5) yield a magnetic field of an equatorial current disk with a finite thickness scale $2D$. The parameters f_i, b_i, and c_i were found by fitting the electric currents obtained as $\nabla \times \nabla \times (A_\phi \mathbf{e}_\phi)/\mu_0$ to the desired profiles of the current density, which have a steep inner edge and different tailward decrease rates at the outer slope of the profile. Note that the vector potential defined by equations (2), (3), (4), and (5) is slightly different from that of *Tsyganenko and Peredo* [1994] (compare their equation(11)), used in the T96 model. In that work, for the sake of simplicity, we chose $b_i = c_i \equiv \beta_i$, while here the parameters b_i and c_i can be varied independently. That made it possible to reduce the number of terms in equation (2) to $N = 5$. We also note a misprint in equations (21) and (22) of *Tsyganenko* [1995], where the parameters g_i should actually read b_i.

[15] To take into account the spatial variation of the current sheet thickness, it suffices to make the parameter D a function of X and Y (before taking the curl of **A**). It was assumed as

$$D = D_0 + \Delta D_y \left(\frac{Y}{\Delta Y}\right)^2 + \Delta D_x \exp\left(\frac{X}{\Delta X}\right), \tag{6}$$

providing a sunward and dawn/duskward flaring of the current sheet, controlled by the parameters ΔD_x, ΔX, and ΔD_y (ΔY enters as a factor by ΔD_y and hence can be kept fixed). The sunward flaring, given by the last term in equation (6), affects only the dayside part of the current disk, located outside the magnetosphere, and has virtually no effect on the tail field. The only purpose of that term is to reduce the gradient of the unshielded field of the current disk in the subsolar region and thus avoid excessively long expansions for the tail shielding field, as discussed in detail in section 2.4.2.1.

[16] Partial tail field terms with different scale lengths of the tailward decrease of the current density can be generated from the basic form of equations (2), (3), (4), and (5) by simple transformations of coordinates. These transformations combine a uniform shift of the entire current system along the X axis (keeping unchanged the position of the inner edge of the current sheet) with suitable scaling, that is, replacing the original coordinates {X, Y, Z} with {$\eta X - (\eta - 1)X_m$, ηY, ηZ}, where X_m is the position of the peak of the electric current density and η is the scaling factor. To keep the value of the sheet thickness independent of that scaling factor, it is also necessary to replace D by ηD. In addition, one can introduce a variable shift X_s of the current sheet along the Sun-Earth line, as another free parameter of the model.

[17] Table 1 contains the values of the parameters f_i, b_i, and c_i, and Figure 1 shows two profiles of the electric

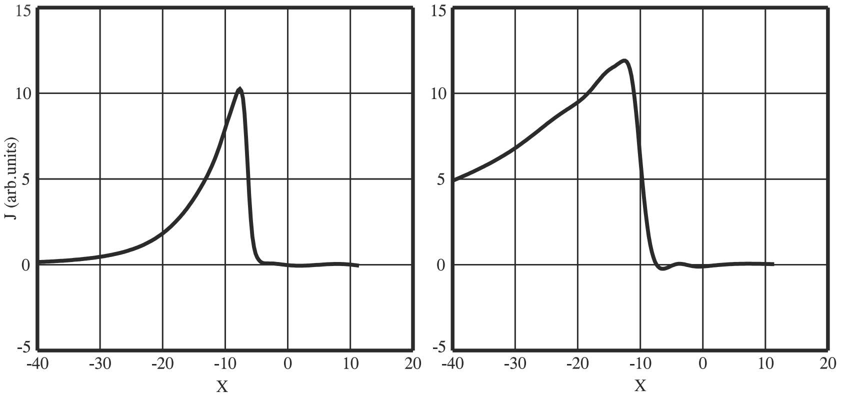

Figure 1. Variation of the electric current density in the model cross-tail current sheet along the X_{GSM} axis for the two modules with different rates of the tailward falloff: (left) the "short" near-tail module and (right) the "long" module.

current density along the Sun-Earth line for two tail field modules with different rates of the tailward falloff of J_y. The plots correspond to the following values of the parameters: $\eta = 1.1$, $X_m = -12$, and $X_s = 6$ for the "short" module, and $\eta = 0.25$, $X_m = -12$, and $X_s = 4$ for the "long" one. These two modules are among the building blocks of the model, described here and in Paper 2.

2.2.2. Including the tilt-related deformation

[18] The next step is to incorporate dipole tilt effects in the tail field model. Here this is done by applying the deformation method [*Stern*, 1987; *Tsyganenko*, 1998, hereinafter referred to as T98] to the untilted configuration, an approach combining a great flexibility with simplicity and clarity. It is important to note that the deformation is applied to the total field of the tail current, including its shielding field. As shown in detail in T98, the dipole tilt effect on the shape of the tail current sheet can be introduced as a superposition of two deformations.

[19] The first deformation modifies the angular coordinate $\varphi = \arctan(Z_{\mathrm{GSM}}/Y_{\mathrm{GSM}})$, which results in a warping of the current sheet in the *Y-Z* plane. Owing to the axial symmetry of the original (undeformed) magnetopause, its shape is not affected by the deformation, and the total tail field remains fully shielded within the boundary. A detailed description of the procedure has been given elsewhere (T98, equations 13 and 14); for the sake of completeness and to avoid possible confusion about the notation of variables, it is reproduced in equations (7), (8), (9), and (10) below.

[20] The original angular coordinate φ is replaced by

$$F = \varphi + G\frac{\varrho^3\cos\varphi}{\varrho^4 + L_4}\sin\Psi \tag{7}$$

where Ψ is the dipole tilt angle, $\varrho = \sqrt{Y^2 + Z^2}$, the parameter G defines the warping amplitude, and L is a scale size, quantifying the spatial extent of the warping across the tail and hence the curvature of the warped current sheet in the *Y-Z* cross section. In general, both G and L vary with the tailward distance; a data-based quantitative study of that effect was made in our earlier work [*Tsyganenko et al.*, 1998, Table 1]. In principle, we could use the results of that work for specifying G and L as functions of X_{GSM}; however, since the present model covers only a limited part of the near tail, in this work, G and L were considered as constant parameters, and their values were found by fitting of the model to data by least squares, as described in detail in Paper 2.

[21] Having thus defined the modified angle F, we have the deformed Cartesian coordinates as

$$Y^* = \varrho\cos F,$$
$$Z^* = \varrho\sin F,$$

and calculate the Cartesian components of undeformed field at the deformed location as $B_x^* = B_x(X, Y^*, Z^*)$, $B_y^* = B_y(X, Y^*, Z^*)$, and $B_z^* = B_z(X, Y^*, Z^*)$, from which we have the cylindrical components

$$\begin{aligned} B_\varrho^* &= B_y^*\cos F + B_z^*\sin F,\\ B_\varphi^* &= -B_y^*\sin F + B_z^*\cos F. \end{aligned} \tag{8}$$

Next, we derive the cylindrical components of the deformed field (T98, equation 13) as

$$\begin{aligned} B_\varrho' &= B_\varrho^*\frac{\partial F}{\partial\varphi},\\ B_\varphi' &= B_\varphi^* - \varrho\left[B_x^*\frac{\partial F}{\partial X} + B_\varrho^*\frac{\partial F}{\partial\varrho}\right],\\ B_x' &= B_x^*\frac{\partial F}{\partial\varphi}, \end{aligned} \tag{9}$$

and finally convert B_ϱ' and B_φ' to B_y' and B_z':

$$\begin{aligned} B_y' &= B_\varrho'\cos\varphi - B_\varphi'\sin\varphi,\\ B_z' &= B_\varrho'\sin\varphi + B_\varphi'\cos\varphi. \end{aligned} \tag{10}$$

[22] The second deformation is a radially dependent rotation around the Y axis, which causes the tail current sheet to bend in the *X-Z* plane, so that it tilts with the dipole in the inner/near magnetosphere and shifts in the north-south direction in the distant tail. Unlike the first one, this deformation affects the shape of the model magnetopause. Namely, as discussed in more detail in T98, it results in a north-south displacement of the tailward part of the magnetopause, so that it shifts toward positive (negative) Z_{GSM} for $\Psi > 0$ ($\Psi < 0$), in agreement with direct magnetopause observations.

[23] The deformation is applied to Cartesian GSM coordinates, so that a point (X, Y, Z) is rotated around the Y axis by an angle $\Psi^*(r)$, gradually decreasing with growing radial distance r, and maps to a new position (X^*, Y^*, Z^*), so that

$$\begin{aligned} X^* &= X\cos\Psi^*(r) - Z\sin\Psi^*(r),\\ Y^* &= Y,\\ Z^* &= X\sin\Psi^*(r) + Z\cos\Psi^*(r). \end{aligned} \tag{11}$$

The rotation angle $\Psi^*(r)$ is given by

$$\sin\Psi^* = \frac{R_H\sin\Psi}{(R_H^3 + r^3)^{1/3}}. \tag{12}$$

This yields $\Psi^* \approx \Psi$ near Earth, while at large distances, $\sin\Psi^* \sim \sin\Psi\,(R_H/r)$. As shown in T98, the hinging distance R_H itself can be assumed to be a function of position, replicating the observed weaker response of the magnetopause position to the dipole tilt angle, than that of the cross-tail current sheet. In this model we assumed

$$R_H = R_{H0} + R_{H2}\frac{Z^2}{r^2}, \tag{13}$$

where $R_{H0} = 8.95\ R_E$ was found from least squares fitting (see Paper 2) and $R_{H2} = -5.2\ R_E$ was specified to provide the observed amplitude of the tilt-related shift of the magnetotail boundary at $X \sim -30\ R_E$, as obtained in T98.

[24] The final equations for the components of the deformed field read as follows:

$$B'_x = B^*_x \frac{\partial Z^*}{\partial Z} + B^*_y\left(\frac{\partial X^*}{\partial X}\frac{\partial Z^*}{\partial Z} - \frac{\partial X^*}{\partial Y}\frac{\partial Z^*}{\partial Z}\right) - B^*_z\frac{\partial X^*}{\partial Z},$$

$$B'_y = B^*_y\left(\frac{\partial X^*}{\partial X}\frac{\partial Z^*}{\partial Z} - \frac{\partial X^*}{\partial Z}\frac{\partial Z^*}{\partial X}\right), \tag{14}$$

$$B'_z = -B^*_x \frac{\partial Z^*}{\partial X} + B^*_y\left(\frac{\partial Z^*}{\partial X}\frac{\partial X^*}{\partial Y} - \frac{\partial X^*}{\partial X}\frac{\partial Z^*}{\partial Y}\right) + B^*_z\frac{\partial X^*}{\partial X}.$$

Here the starred field components are defined by $\mathbf{B}^* \equiv \mathbf{B}(X^*, Y^*, Z^*)$, the deformed coordinates $\{X^*, Y^*, Z^*\}$ are given by equation (11), and their partial derivatives are calculated taking into account the radial variation of Ψ^* from equation (12) and R_H from equation (13).

2.3. Modeling the Field of the Birkeland Currents

[25] Data-based modeling of the magnetic fields from the Region 1 and 2 Birkeland currents on a global scale has been a stubbornly difficult problem for many years, in part because of their complex geometry and also because of the lack of information on their sources and closure path in the distant magnetosphere. *Tsyganenko and Stern* [1996] devised an empirical approximation, based on a statistical pattern of field-aligned currents at low altitudes, and its mapping to the distant magnetosphere along geomagnetic field lines in an average model magnetosphere. A serious deficiency of that model was its insufficient flexibility; in particular, it did not allow one to vary the azimuthal distribution of the currents and the size of the Region 1/2 ovals, so that the only variable parameter was the total magnitude of the current. Another drawback was the somewhat cumbersome way of representing the field, requiring three separate approximations: in the low-latitude region, inside the Birkeland current sheet, and in the high-latitude magnetosphere.

[26] In this work a new model has been developed, removing the above limitations. In brief, the overall calculation scheme was as follows. The first step was to numerically calculate "partial" global field distributions generated by Birkeland currents (either Region 1 or 2), flowing on an axially symmetric surface and with their local time variation of the current density expanded in Fourier harmonics, that is, as sines and/or cosines of multiples of the solar-magnetic longitude.

[27] The next step was to find suitable analytical approximations for those partial fields, so that the total field could be represented as their linear combination, allowing one to derive the local time variation of Birkeland currents by fitting the model to data. Such approximations were obtained, using simple analytical model fields of a conical current sheet with a finite width, developed in our earlier work [*Tsyganenko*, 1991]. To make the behavior of the model field agree with the numerically computed one, the conical harmonics were modified by a suitable deformation, whose parameters yielded a best fit of the deformed field to the numerical results.

[28] The above calculations, however, provided the field produced only by the northern part of the field-aligned current system. Assuming that (for zero tilt angle of the geodipole) the southern currents are symmetric to the northern ones, their magnetic field can be easily obtained as a mirror reflection of the field from the northern currents by appropriately changing the signs of the coordinates and of the field components.

[29] After that, two more deformations were applied to the net field of the northern and southern Birkeland currents, to introduce the observed noon-midnight asymmetry of the Birkeland currents and to take into account the effect of the dipole tilt angle upon their geometry. Then a uniform scaling was introduced, to replicate the observed expansions and contractions of the Region 1 and 2 ovals. Finally, a shielding field was derived, in order to confine the model field within the magnetopause. A detailed description of the calculations at each step is given below.

2.3.1. Numerical calculation of the axisymmetric Birkeland current field

[30] Our intent in choosing an axially symmetric shape of the Birkeland current sheet as a starting approximation was to reduce the three-dimensional (3-D) problem to a two-dimensional (2-D) one. This greatly simplifies the calculation, thanks to an important general property of such electric current systems. Namely, as shown earlier [*Tsyganenko*, 1993, Appendix B], if a current flows on an axisymmetric surface and its components vary with the azimuthal angle as cos $m\phi$ and sin $m\phi$, then the expansions of the components of its magnetic field contain only Fourier terms of the same mth order. Therefore the magnetic field in all of space can be readily obtained by calculating contributions from individual harmonics in only one meridional plane, since their local time variation is known to follow either cos $m\phi$ or sin $m\phi$.

[31] The initial configuration of the Birkeland current sheets was defined as following an axially symmetric surface

$$\Theta(r) = \arcsin\left[\frac{\sqrt{r}}{\left(r^n + \sin^{-2n}\theta_0 - 1\right)^{\frac{1}{2n}}}\right], \tag{15}$$

where r and Θ are geocentric radial distance and solar-magnetic colatitude. The surface (equation (15)) intersects the Earth's surface along a circle $\Theta = \theta_0$, corresponding to the observed average position of the current system it describes (either Region 1 or 2). At low altitudes the current sheet approximately follows a dipolar field line shell with $L = 1/\sin^2\theta_0$. At larger distances its shape reflects the distortion of the outer magnetospheric field, stretched tailward on the nightside. The current flow lines start at low altitudes as field aligned but are not necessarily field aligned at greater distances.

[32] The power index n defines the location of the transition region between the dipole-like and tail-like shape of the meridional cross sections of the surface (equation (15)). On the basis of their comparison with empirical model field lines, whose foot points map onto the low-altitude zones of Birkeland currents, we chose $n = 6$ and $n = 12$ for approximating the Region 1 and 2 current sheets, and the corresponding values of the ground colatitude θ_0 were assumed equal to 15° and 21°, respectively. Figure 2 displays two families of contours $\Theta(r) =$ constant, corresponding to the above values of n, and the heavy solid lines indicate the assumed initial configuration of the field-aligned current sheets.

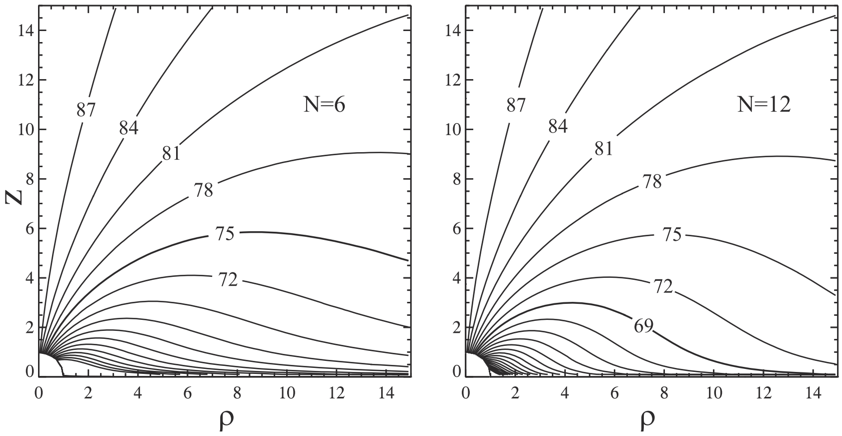

Figure 2. Contours of constant values of the function $\Theta(r, \theta_0)$, for different values of the foot point colatitude θ_0. The two panels correspond to (left) $n = 6$ and (right) $n = 12$; the heavy lines on the plots show the shape of the surfaces, used for approximating the Region 1 and 2 field-aligned current sheets, respectively.

[33] In general, the present approximation for the shape of the model Birkeland current sheet is similar to that adopted in the T96 model for the Region 1 current system (note that equation (15) is equivalent to equation (2) of *Tsyganenko and Stern* [1996]). A difference is that here we introduce the day-night asymmetry by using a deformation of an initially axisymmetric field, while in T96 that asymmetry was present in the model from the outset, since the colatitude θ_0 was assumed to vary with the longitude ϕ. The choice of flow line geometry rests in part on guesses and approximations, such as the assumption that they all lie in meridional planes, discussed below. However, observations currently available do not allow more details to be included.

[34] Having defined the shape of the sheet, one can uniquely specify the electric current at any location by defining its longitudinal profile at ionospheric altitude and by making an additional assumption that its azimuthal component is zero at all distances, which means that individual current flow lines are contained within meridian planes and extend all the way to infinity (in the initial unshielded model). This assumption implies that on the nightside the Region 1 currents map into the distant tail, flowing in the vicinity of the plasma sheet boundary layer, while on the dayside and in the dawn/dusk sectors they extend to the magnetopause. As in the case of the cross-tail current, adding the shielding field and nullifying the total field outside the magnetosphere results in a redirection of the initially unbounded Birkeland currents, so that they become closed via the magnetopause [*Tsyganenko and Stern*, 1996, section 2.1]. More details on that question are given in section 2.4.2.3. The model Region 2 currents differ from those of Region 1 in that they map to lower latitudes in the magnetosphere and smoothly blend there with the ring and magnetotail currents, in line with the concept of their origin due to the nightside plasma convection. It should be noted that the Region 2 Birkeland currents and the field-aligned currents associated with the PRC are driven by essentially the same physical mechanism, that is, by the sunward plasma convection on the nightside. However, for the sake of mathematical tractability we introduced them here separately, so that the PRC represents the innermost part of the system, while the model Region 2 currents flow from and to the near-tail plasma sheet.

[35] At the ionospheric altitude the strength of the current for *m*th individual mode varies with longitude as $\sin m\phi$. The principal mode ($m = 1$) corresponds to a downward (upward) Region 1 (Region 2) current in the dawn sector and an upward (downward) current in the dusk sector, respectively. The second harmonic ($m = 2$) provides currents of opposite polarities within both dawn and dusk sectors, allowing one to take into account a possible noon-midnight asymmetry of the Birkeland currents. The magnitude of the currents was normalized in such a way that in each hemisphere the net current per one half-wave of each sinusoidal mode (i.e., between $\phi = 0°$ and $\phi = 180°$ for $m = 1$ and between $\phi = 0°$ and $\phi = 90°$ for $m = 2$) equals 10^6 A.

[36] Having thus defined the electric current distributions for individual modes, we use the Biot-Savart integral to calculate the components of the magnetic field. The integration was performed by dividing the circular zone of field-aligned currents at $r = 1\ R_E$ into 200 1.8° intervals of longitude. To take into account a finite latitudinal thickness of the current sheet (assumed equal to 3.5° for Region 1 and 5.2° for Region 2), each of the longitudinal intervals was divided into 11 intervals of latitude. Integration was conducted along each of the elementary current flow line tubes, extending from Earth's center to a distance of $r = 200\ R_E$, i.e., well beyond the modeling region, so that the effect of the remote closure currents could be neglected.

[37] At low altitudes the field-aligned currents actually close via the ionosphere, rather than through the Earth's center. However, as concerns the model magnetic field inaccuracy, the difference between the geocentric and ionospheric closure becomes perceptible only at the Earth's surface and within a few hundred kilometers above it, and has no significant effect on magnetospheric field line mapping. A more quantitative analysis of that aspect is given in section 2.3.4.

[38] Owing to the property of axially symmetric current sheets, mentioned in the beginning of this section, the

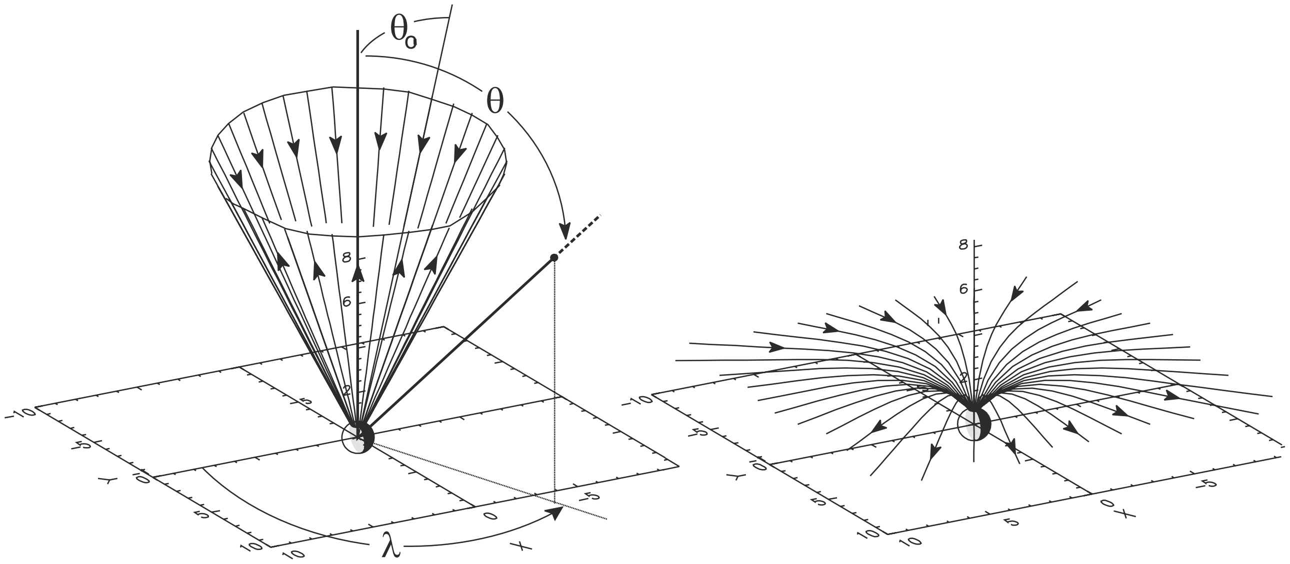

Figure 3. Illustration of the geometry of the model Birkeland currents: (left) a conical current sheet, whose magnetic field is given by the analytical vector potential (equations (16) and (17)) [*Tsyganenko*, 1991], and (right) a deformed conical sheet, in which the currents near Earth flow along dipolar magnetic field lines.

magnetic field distribution had to be numerically calculated in only one meridional plane, at a grid of points covering the range of distances between $r = 1\ R_E$ and $r = 40\ R_E$. Since the field vectors were to be used to derive an analytical approximation in the entire 3-D space, it was necessary to ensure that all components of **B** have comparable magnitudes; for that reason the longitude of the calculation plane was chosen at $\phi = 45°$ for the mode with $m = 1$ and at $\phi = 22.5°$ for $m = 2$. To avoid singularity of the integrand, the interior of the current sheet was excluded from the Biot-Savart calculations. In doing so, we tacitly assumed that the approximation procedure (section 2.3.2) would provide a sufficiently accurate smooth interpolation of the field components inside the current sheet. Testing of the analytical model (section 2.3.3 and Figures 4 and 5) confirmed the expected results.

[39] In this modeling effort, only two harmonic terms with $m = 1$ and $m = 2$ were used in each of the two Birkeland current systems (Regions 1 and 2). As shown in Paper 2, this is sufficient for extracting from the data the most essential information on the asymmetry between the day and night parts of the field-aligned current zones.

2.3.2. Approximating the numerically computed field

[40] To approximate the results of the numerical calculation by a continuous and divergence-free analytical field, we turned to "conical" harmonics, first introduced in our early effort to build a field model for field-aligned currents [*Tsyganenko*, 1991]. In that work the magnetic field was represented in spherical coordinates as the curl of a vector potential having only a radial component A_r, approximated by a sum of longitudinal Fourier modes:

$$A_r = \sum_{m=1}^{N} B_m A^{(m)}(\theta, \phi) = \sum_{m=1}^{N} B_m T^{(m)} \sin m\phi, \qquad (16)$$

where the piecewise-continuous functions $T^{(m)}$ read as follows:

$$T^{(m)}(\theta) = \begin{cases} \tan^m \frac{\theta}{2} & \text{for } \theta < \theta^-, \\ \frac{1}{\tan\frac{\theta^+}{2} - \tan\frac{\theta^-}{2}} \tan^m \frac{\theta}{2} \left(\tan\frac{\theta^+}{2} - \tan\frac{\theta}{2} \right) & \\ + \frac{\tan^{2m+1}\frac{\theta}{2} - \tan^{2m+1}\frac{\theta^-}{2}}{(2m+1)\tan^m\frac{\theta}{2}} & \\ & \text{for } \theta^- \le \theta \le \theta^+, \\ \frac{\tan^{2m+1}\frac{\theta^+}{2} - \tan^{2m+1}\frac{\theta^-}{2}}{(2m+1)\left(\tan\frac{\theta^+}{2} - \tan\frac{\theta^-}{2}\right)} \cot^m \frac{\theta}{2} & \\ & \text{for } \theta > \theta^+. \end{cases} \qquad (17)$$

Equations (16) and (17) describe a magnetic field of purely radial currents flowing within a conical current sheet with a finite thickness $2\Delta\theta$, whose inner and outer boundaries are specified by the colatitudes $\theta^- = \theta_0 - \Delta\theta$ and $\theta^+ = \theta_0 + \Delta\theta$, respectively, as illustrated in Figure 3. The mode number m defines the longitudinal structure of the currents in exactly the same way as in the above numerical model, so that $m = 1$ yields the principal mode with downward current on the dawnside and upward one on the duskside (or vice versa), peaking at $\phi = \pm\pi/2$.

[41] Although the model (equations (16) and (17)) replicates fairly well the effects of Birkeland currents just above the ionosphere, it yields grossly inaccurate results at larger distances, because the geometry of the conical current sheet is very different from the actual one, in which the currents flow into and out of the ionosphere along dipolar field lines. In quantitative terms the magnetic field in the conical model falls off with the radial distance as $B \sim r^{-1}$, whereas a more realistic model with a dipolar shape of the electric current flow lines yields $B \sim r^{-3/2}$ [*Tsyganenko*, 1990]. Incidentally, this is one of the reasons why the conical model cannot be directly used for evaluating the contribution of

Table 2. Parameters of the Model Magnetic Field of Region 1 and 2 Birkeland Currents, Entering in Equations (18) and (19)

	Region 1		Region 2	
	$m = 1$	$m = 2$	$m = 1$	$m = 2$
B_m	0.1618068	0.7058027	0.1278764	0.4036015
θ_0	0.7113545	0.5567714	0.8867880	0.7247997
a_1	−0.1797958	−0.2845939	−0.2320034	−0.3302974
a_2	2.999643	5.715471	1.805623	2.827731
a_3	−0.9322709	−2.472821	−32.37241	−45.44406
a_4	−0.6811060	−0.7738802	−0.9931491	−1.611104
a_5	0.2099057	0.3478294	0.3175086	0.4927112
a_6	−8.358816	−11.37654	−2.492466	−0.00325846
a_7	−14.86034	−38.64769	−16.21600	−49.59015
a_8	0.3838363	0.6932928	0.2695393	0.3796217
a_9	−16.30946	−212.4017	−6.752691	−233.7884
b_1	4.537023	4.944205	3.971795	4.312667
b_2	2.685836	3.071270	14.54478	18.05052
b_3	27.97833	33.05882	41.10158	28.95320
b_4	6.330871	7.387534	7.912890	11.09948
b_5	1.876532	2.366769	1.258297	.7471650
b_6	18.95619	79.22573	9.583548	67.10246
c_1	0.9651528	0.6154290	1.014142	0.5667097
c_2	0.4217195	0.5592051	0.5104135	0.6468520
c_3	−0.0895777	−0.1796585	−0.1790431	−0.1560666
c_4	−1.823556	−1.654932	−1.756358	−1.460805
c_5	0.7457045	0.7309109	0.7561987	0.7719654
c_6	−0.5785917	−0.4926293	−0.6775248	−0.6658989
c_7	−1.010201	−1.130266	−.04014016	0.251518E-5
c_8	0.0111239	−0.00961398	0.0144680	0.0242602
c_9	0.0957293	0.1484586	0.1200522	0.1195003
c_{10}	−0.3599292	−0.2215347	−0.2203585	−0.2625739
d_1	8.713701	7.883593	4.508964	4.377173
d_2	0.9763933	0.02768252	0.8221624	0.2421191
d_3	3.834603	2.950281	1.779934	2.503483
d_4	2.492118	1.212635	1.102650	1.071587
$\langle B \rangle$	13.18	14.01	11.43	12.94
$\langle \Delta B \rangle$	0.43	0.37	0.52	0.61

Birkeland currents in the distant magnetosphere, as was done in a recent work by *Alexeev et al.* [2000]. Our earlier work [*Tsyganenko*, 1991] attempted to take into account the actual geometry of the Birkeland currents by warping the original conical surface; however, that warping left intact the magnetic field outside the current sheet and hence could not remedy the problem.

[42] An effective solution, overlooked in the above mentioned efforts, is to modify the conical field (equations (16) and (17)) by applying to it a suitable deformation. As illustrated in Figure 3, it is intuitively clear that the needed deformation should provide a partial "eversion" of space, for example, by stretching the coordinate θ in the Northern Hemisphere, accompanied by its contraction in the Southern Hemisphere. Unfortunately, there is no straightforward method to directly determine the necessary deformation, and the deformed magnetic field can be quite sensitive to the details of the coordinate transformation. For that reason our approach here was to define a flexible analytical deformation of spherical coordinates with many free parameters and then fit their values by least squares, to minimize the rms difference between the deformed conical field and the one obtained by the Biot-Savart integral. The method proved an effective tool, and the rest of this is devoted to details of the calculation.

[43] The desired deformation of the spherical coordinates r and θ was sought as a sum of terms, satisfying appropriate symmetry requirements and with different dependence on the original coordinates. Having tested many trial versions, we chose the following coordinate transformation:

$$
\begin{aligned}
r' = r &+ \frac{a_1}{r} + a_2 \frac{r}{\sqrt{r^2 + b_1^2}} + a_3 \frac{r}{r^2 + b_2^2} \\
&+ \left(a_4 + \frac{a_5}{r + a_6} \frac{r}{\sqrt{r^2 + b_3^2}} + a_7 \frac{r}{r^2 + b_4^2} \right) \cos\theta \\
&+ \left(a_8 \frac{r}{\sqrt{r^2 + b_5^2}} + a_9 \frac{r}{r^2 + b_6^2} \right) \cos 2\theta,
\end{aligned}
\qquad (18)
$$

$$
\begin{aligned}
\theta' = \theta &+ \left(c_1 + \frac{c_2}{r} + \frac{c_3}{r^2} + c_4 \frac{r}{\sqrt{r^2 + d_1^2}} \right) \sin\theta \\
&+ \left(c_5 + \frac{c_6 r}{\sqrt{r^2 + d_2^2}} + \frac{c_7 r}{r^2 + d_3^2} \right) \sin 2\theta \\
&+ \left(c_8 + \frac{c_9}{r} + \frac{c_{10} r}{r^2 + d_4^2} \right) \sin 3\theta.
\end{aligned}
\qquad (19)
$$

The approximation of equations (16), (17), (18), and (19) yielded a sufficiently accurate fit of the Fourier modes with $m = 1$ and $m = 2$ for both the Region 1 and 2 fields, providing four sets of the parameters in equations (18) and (19). Their values are given in Table 2, which also displays the values of the overall magnitude coefficient B_m, initial cone apex angle θ_0 (Figure 3), rms magnitudes of the model field $\langle B \rangle$, and its rms deviations $\langle \Delta B \rangle$ with respect to the Biot-Savart field.

[44] By construction, the above described model provided the global field, produced only by the northern part of the entire Birkeland current system. The contribution from the southern currents (symmetric to the northern ones for $\Psi = 0$) can be readily represented by rotating the northern (N) part by 180deg around the X-axis and changing the polarity of the current, so that the total field is

$$
\begin{aligned}
B_x(X,\ Y,\ Z) &= B_x^{(N)}(X,\ Y,\ Z) - B_x^{(N)}(X,\ -Y,\ -Z), \\
B_y(X,\ Y,\ Z) &= B_y^{(N)}(X,\ Y,\ Z) + B_y^{(N)}(X,\ -Y,\ -Z), \\
B_z(X,\ Y,\ Z) &= B_z^{(N)}(X,\ Y,\ Z) + B_z^{(N)}(X,\ -Y,\ -Z).
\end{aligned}
\qquad (20)
$$

As pointed out earlier [*Stern*, 1994; *Tsyganenko*, 1998], the deformation method should be used with caution, since it does not conserve the electric current density. In the above procedure the effect of the unphysical currents due to the deformation of the original conical current sheet was minimized, owing to the fact that the deformed field was accurately fitted to the numerically computed Biot-Savart field (which is strictly curl-free outside of the current sheet).

2.3.3. Modeling the noon-midnight asymmetry, dipole tilt effects, and spatial scaling

[45] As was established by the first statistical studies of the Birkeland currents [*Iijima and Potemra*, 1976, 1978], the centers of the Regions 1 and 2 are shifted to the nightside, reflecting the basic day-night asymmetry of the entire magnetosphere, in which the nightside field lines from the auroral oval go to the tail plasma sheet, while its dayside part maps to high latitudes and is associated with the polar cusps. Another effect to be replicated by a model is a tilt-related deformation of the entire current system, including a seasonal/diurnal motion of the zones of field-aligned currents at low altitudes, resulting in

their equatorward shift in winter and a poleward shift in summer. Finally, the model should include additional freedom to reproduce the large-scale spatial redistribution of the Birkeland currents in response to changing interplanetary conditions.

[46] A simple way to include the day-night asymmetry and the tilt-related effects is to apply another deformation to the magnetic field, by modifying the azimuthal angle φ in a cylindrical coordinate system, co-axial with the Y_{GSM} axis. An important requirement here is that the deformations should be relatively small and sufficiently smooth, to keep the field outside the warped current sheets approximately curl-free.

[47] Mathematically, the procedure is similar to the tilt-related deformation of the tail field, described in section 2.2.2, so that the transformation equations have the same form as equations (8), (9), and (10) but with some differences. First, the rotation now occurs around the Y axis, rather than around X, so we redefine $\varrho = \sqrt{X^2 + Z^2}$ and $\varphi = -\arctan(Z_{\mathrm{GSM}}/X_{\mathrm{GSM}})$. Second, the function F representing the deformation in φ is somewhat different from the one in equation (7), because of the following considerations. It is intuitively clear that the desired effect can be achieved by stretching the coordinate φ on the dayside and shrinking it on the nightside. To make the pattern near Earth shift with the tilt of the dipole, we add a separate term, providing a nearly complete "dragging" of the deformed coordinate F at low altitudes, with a gradual decrease of that effect at larger distances. A simple stretch transformation

$$F = \varphi - \left(\Delta\varphi + b\frac{\varrho^2 - 1}{\varrho^2 + \varrho_0^2}\right)\sin\varphi - \frac{\beta\Psi}{\left[1 + \left(\frac{r-1}{R_H}\right)^{\epsilon}\right]^{\frac{1}{\epsilon}}} \tag{21}$$

yields the needed result. Here the second term in the right-hand side provides the required shift of the field-aligned current oval to the nightside, and the third one yields the tilt-related effect. The parameter $\Delta\varphi$ controls the degree of the nightside shift at low altitudes, while b and $_0$ define the amplitude of the deformation at large distances and the rate of its increase with the distance from the Y axis. In the first trial version of the model, we assumed $\Delta\varphi = 0.055$ and $\Delta\varphi = 0.030$ for the Region 1 and 2 currents, respectively, so that at the ionospheric altitude they shift by $\approx$3.2° and $\approx$1.7° to the nightside. Two other parameters in the second term of equation (21) were set at $b = 0.5$, and $\varrho_0 = 7.0\ R_E$, so that in the distant magnetosphere the Region 1 currents map to an average location of the polar cusp on the dayside and to the plasma sheet boundary layer on the nightside.

[48] The tilt-related parameter β defines a "slippage" between Earth and the Birkeland current oval; the assumed value $\beta = 0.9$ yields a shift of $\approx$ 3.5° for the maximal value of the dipole tilt $\Psi = 35°$, which roughly corresponds to observations [*Newell and Meng*, 1989] and to empirical modeling [*Tsyganenko*, 1990]. The parameter R_H is a "hinging distance," defining the radial extent of the inner region dominated by the "dragging" effect of the dipole tilt. It is similar to an analogous quantity in equation (12) of section 2.2.2, describing the tilt-induced deformations of the magnetopause and of the tail current sheet. Here its value was set equal to 10 R_E. The parameter ϵ defines the radial distribution of the tilt-related deformation; as shown in T98 (section 3), it is reasonable to assume $\epsilon = 3$.

[49] Accordingly, $X^* = \varrho \cos F$, $Z^* = -\sin F$, and the cylindrical components of the "starred" field $\mathbf{B}^* = \mathbf{B}(X^*, Y, Z^*)$ are

$$\begin{aligned} B_\varrho^* &= -B_x^* \cos F - B_z^* \sin F, \\ B_\varphi^* &= -B_x^* \sin F - B_z \cos F. \end{aligned} \tag{22}$$

The components of deformed field then read

$$\begin{aligned} B'_\varrho &= B_\varrho^* \frac{\partial F}{\partial \varphi}, \\ B'_\varphi &= B_\varphi^* - \varrho\left[B_y^* \frac{\partial F}{\partial Y} + B_\varrho^* \frac{\partial F}{\partial \varrho}\right], \\ B'_z &= B_y^* \frac{\partial F}{\partial \varphi}, \end{aligned} \tag{23}$$

and, finally, in the original Cartesian system

$$\begin{aligned} B'_x &= B'_\varrho \cos\varphi - B'_\varphi \sin\varphi, \\ B'_z &= -B'_\varrho \sin\varphi - B'_\varphi \cos\varphi. \end{aligned} \tag{24}$$

The above equations are, in general, similar to equations (8), (9), and (10), except for the difference due to the different orientation of the axes.

[50] As concerns the solar wind and IMF effects on the spatial configuration of the field-aligned currents, a fundamental mode of response to a growing disturbance level is an overall equatorward expansion of the auroral and Birkeland current ovals, accompanied by a deeper penetration of magnetospheric plasma into the inner magnetosphere. This prompted us to introduce a simple spatial scaling of the field from the Birkeland currents with the scaling factor a free model parameter. The procedure is similar to the one used for the ring current (section 2.1); however, that case did not include any renormalization factor, so that the field at Earth's surface produced by the ring current did not depend on its size. In contrast, here we chose the total Birkeland current flowing into the ionosphere (and flowing out of it) as an independent model parameter. One can easily verify that in order for that current to be independent of the spatial scaling factor ζ, the following renormalization of the scaled field is needed:

$$\mathbf{B}'_{\mathrm{FAC}}(\mathbf{r}) = \zeta \mathbf{B}_{\mathrm{FAC}}(\zeta\, \mathbf{r}). \tag{25}$$

[51] Figure 4 illustrates the geometry of the model Birkeland currents, in particular, their noon-midnight asymmetry, as a color-coded plot of the electric current density, calculated as the curl of the model field near the noon-midnight meridian plane. Since the field-aligned currents in this model, by construction, are antisymmetric with respect to the plane $Y = 0$ (and hence the current density vanishes in that plane), the plots were actually generated in the plane $\phi = 10°/\phi = 190°$, slightly rotated off the noon-midnight meridian.

[52] Figure 5 shows polar plots of the field-aligned current density at the ionospheric altitude, corresponding to two Fourier modes ($m = 1$ and $m = 2$) of the model Region 1 and 2 systems. In this particular case the Region 1

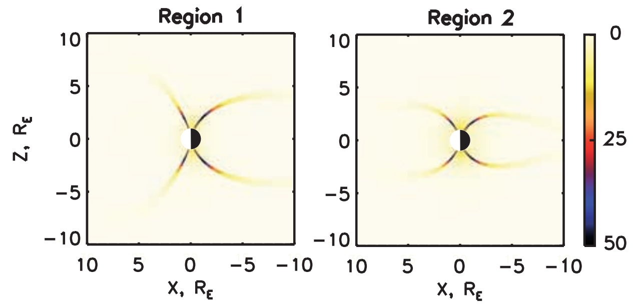

Figure 4. Distribution of the electric current density in the model Region 1 and 2 Birkeland currents in the meridional plane $\phi = 10°/\phi = 190°$, demonstrating their radial variation and day-night asymmetry. The currents were calculated as the curl of the model magnetic field; the color coding is in arbitrary units. Note a dramatic increase of the current density near Earth owing to the convergence of the magnetic field lines.

currents map to the latitudes 76° and 70° on the dayside and nightside, respectively, while for the Region 2 currents the corresponding latitudes are equal to 69° and 65°. By varying the scaling parameters the current systems can be shifted to lower or higher latitudes, both in the ionosphere and at larger distances. As described in section 2.4.2.3, an appropriate modification has also been made to the corresponding shielding fields, so that the total field remains confined within the magnetopause in a sufficiently wide range of values of the scaling parameters.

[53] In the present model the Birkeland currents, by construction, are symmetric with respect to the noon-midnight plane. This restriction does not allow us to take into account the observed longitudinal rotation of the Region 1 current pattern during periods with strong IMF B_y [e.g., *Erlandson et al.*, 1988; *Zhou et al.*, 2000]. Such a rotation can, in principle, be modeled by introducing in the expansion (equation (16)) Fourier modes with cos $m\phi$ and adding appropriate terms in the shielding field. Another possible effect is a seasonal variation of the strength of the Region 1 current due to changes in the ionospheric conductivity, which can easily be taken into account by introducing a modulation of the terms in the right-hand side of equation (20) by the dipole tilt angle. Finally, one cannot rule out a possible interhemispheric current, owing to the Z component of the interplanetary electric field due to the IMF B_y [*Leontyev and Lyatsky*, 1974]. This effect can also be taken into account by a simple extension of the vector potential (equation (16)), adding a uniform downward or upward current to the undeformed conical current sheet. We chose not to pursue all these modifications in the present work and plan to address them in a separate detailed study.

2.3.4. On the ionospheric closure of the model Birkeland currents

[54] As already mentioned above, the model Birkeland currents have been assumed to pierce the ionosphere and extend all the way to the Earth's center, while they actually should close via ionospheric currents. Since the corresponding differential current system (i.e., obtained by subtracting the model currents from the actual ones) has a spatial scale size of the order of 1 R_E, it is intuitively clear that the associated inaccuracy of the magnetic field should be significant only at small geocentric distances. To get a more quantitative idea on the relative magnitude of the errors, a similar Biot-Savart integration was made in a model with an ionospheric closure of the Birkeland current. It was assumed that the currents close via the polar cap along dawn-dusk circular arcs, connecting the inflowing and outflowing field-aligned currents in the ionosphere, in the same way as they did in an earlier model [*Tsyganenko and Stern*, 1996].

[55] Figure 6 compares dawn-dusk profiles of three components of the magnetic field of the Region 1 Birkeland current for $Z = 1.2\ R_E$ and $Z = 2.0\ R_E$, where the total strength of the current was assumed equal to 1 MA. Figures 6a and 6b correspond to the first mode (i.e., varying with longitude as $\sim\sin\phi$), and Figures 6c and 6d are for the second mode ($\sim\sin 2\phi$). Even for $Z = 1.2$, there is no major difference between the plots for the geocentric (solid lines) and ionospheric (dashed lines) closure, and the difference almost disappears at $Z = 2\ R_E$. This justifies our choice of the geocentric closure current for the purposes of the modeling of the distant magnetospheric field. Of course, more accurate approximations are needed for an adequate modeling of the field at ionospheric altitudes, which is beyond the scope of this work.

2.4. Model Magnetopause and Representing the Shielding Fields

[56] Following the approach of the T96 model, the model magnetopause was assumed as a given analytical surface

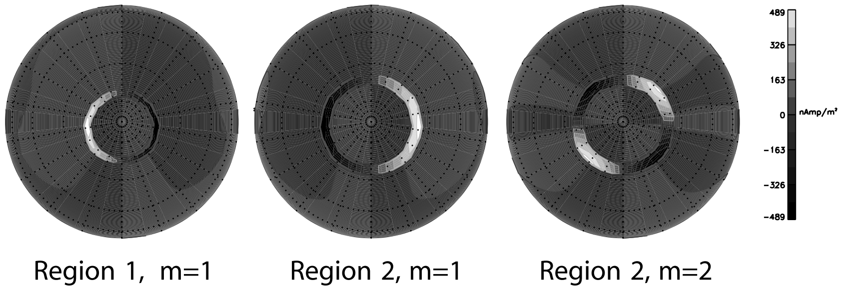

Region 1, m=1 Region 2, m=1 Region 2, m=2

Figure 5. Distribution of the electric current density in the model Region 1 and 2 Birkeland currents at ionospheric altitudes: (left) Region 1, Fourier mode $m = 1$, (middle) Region 2, $m = 1$, and (right) Region 2, $m = 2$. The color coding on the right is given in nA m^2.

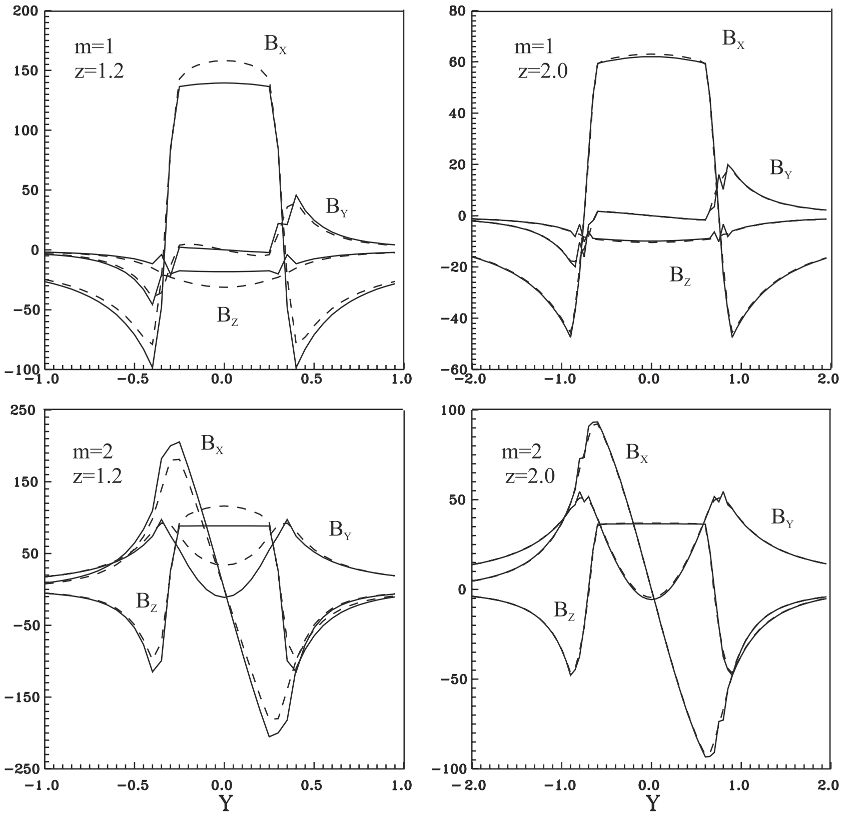

Figure 6. (a-d) Comparing the magnetic field of the model Birkeland currents, closing via the ionosphere (solid lines) with that in the case of the geocentric closure (dashed lines). Figures 6a and 6b (Figures 6c and 6d) correspond to the first (second) longitudinal Fourier modes. Figures 6a and 6c (Figures 6b and 6d) display the variation of three components of **B** vector in the dawn-dusk meridian plane along the line $Z = 1.2\ R_E$ ($Z = 2.0\ R_E$).

with a variable solar wind controlled scale size. Mathematically, the boundary was described as in T96: a prolate hemi-ellipsoid of revolution in front (up to a tailward distance of $\sim 35 R_E$), smoothly extended in the far tail by a cylindrical surface. The difference from T96 is twofold. First, the average shape of the boundary in this work was fitted to the most recent empirical magnetopause of *Shue et al.* [1998], while in the T96 model we used the average magnetopause of *Sibeck et al.* [1991]. Second, on the basis of the observed shift of the nightside magnetopause in the Z direction in response to the geodipole tilt angle (described in section 2.2.2), we introduced a tilt-dependent shape of the boundary, using a method described in detail in T98 and briefly reproduced below.

[57] For the untilted dipole ($\Psi = 0$) the shape of the front part of the boundary is given in GSM coordinates as follows (compare equation (1) of *Tsyganenko* [1995]):

$$\begin{aligned} X &= x_0 - a(1 - \sigma_0 \tau), \\ Y &= a\left(\sigma_0^2 - 1\right)^{1/2}\left(1 - \tau^2\right)^{1/2} \cos\phi, \\ Z &= a\left(\sigma_0^2 - 1\right)^{1/2}\left(1 - \tau^2\right)^{1/2} \sin\phi, \end{aligned} \tag{26}$$

where the ellipsoidal coordinates τ and ϕ span the intervals $0 \le \tau \le 1$ and $0 \le \phi \le 2\pi$ and where the three parameters, x_0, σ_0, and a, are derived by fitting the surface (equation (26)) to an average boundary of *Shue et al.* [1998], with the solar wind ram pressure $P_d = 2$ nPa and IMF $B_z = 0$. The best fit values of the parameters were found equal to $x_0 = 3.486$, $\sigma_0 = 1.198$, and $a = 35.13$, and in the entire region sunward from $X = -30\ R_E$ the rms distance between the two model boundaries (along the normal) did not exceed $\sim 0.2\ R_E$. In principle, we could use the model magnetopause of Shue et al. in its original mathematical form; however, the hemi-ellipsoidal approximation is simpler and more consistent with our numerical algorithms, and that was the main reason for retaining the approximation (equation (26)) for the model boundary.

[58] The tilt-angle effects on the magnetopause shape were taken into account by using a deformation of the boundary (equations (11), (12), (13), and (14)), consistent with the tilt-related warping of the magnetotail field. Its details have already been given above in section 2.2.2.

[59] The main factor defining the size of the magnetopause is the ram pressure of the solar wind, P_d. Although it is known that the magnetopause's reaction to pressure variations depends to a certain extent on the IMF orientation, in the present work we followed the approach of the T96 model and assumed a self-similar compression/expansion of the boundary in response to changes of P_d, scaling its linear dimensions by the factor $\chi = (P_d/\langle P_d \rangle)^{\kappa}$, where $\langle P_d \rangle$ is the average pressure. Simple theory suggests $\kappa \sim 1/6$, but here the power index κ was treated in the trial fitting runs as a free parameter, and a slightly smaller value $\kappa \approx 0.158$ was obtained, as described in more detail in Paper 2. Here we only note that using a self-similar scaling of the boundary

allows one to easily recalculate the shielding field, applying a similar scaling to the spatial distribution of the field components. In particular, the dipole shielding field $\mathbf{B}_{\mathrm{CF}}$ scales as $\mathbf{B}_{\mathrm{CF}}(\mathbf{r}, P_d) = \chi^3\mathbf{B}_{\mathrm{CF}}(\chi\mathbf{r}, \langle P_d\rangle)$.

[60] Another important factor, affecting the shape of the magnetopause, is the IMF orientation. It is known [e.g., *Sibeck et al.*, 1991; *Roelof and Sibeck*, 1993; *Petrinec and Russell*, 1993; *Shue et al.*, 1998] that a negative IMF B_z results in a larger tailward flaring rate of the magnetopause on the nightside. Replicating that effect in the magnetic field models is more difficult, since it requires a change of the shape of the boundary (while the pressure variations affect mainly its size), so that there is no simple recalibration of the shielding fields: a new shape would require us to recalculate anew the shielding fields. For that reason we did not include the IMF effect upon the magnetopause shape in this model and have left it for a future study. This is partly justified by noting that the model was intended primarily to improve the description of the inner magnetospheric field, where the effect of the magnetopause shape variation is of secondary importance.

[61] Once the magnetopause is explicitly defined, we can derive the shielding field $\mathbf{B}_s$ for each individual ("partial") internal-source field $\mathbf{B}_i$, so that the total field $\mathbf{B}_{\mathrm{tot}} = \mathbf{B}_s + \mathbf{B}_i$ remains confined within the boundary for any strength of that current system. Our general approach, similar to that used in the T96 model, was to assume the potential shielding field for an internal field source as the gradient of a flexible scalar potential $U(\mathbf{r}, a_1,\ldots, a_N)$, whose parameters $a_1,\ldots, a_N$ are to be found by minimizing the rms value of the normal component of the total field, $B_n = \mathbf{B}_{\mathrm{tot}}\cdot\mathbf{n}$, over the entire boundary [*Schulz and McNab*, 1987].

[62] As previously shown [*Tsyganenko*, 1995, 1996, 1998], a convenient form of the scalar potential for the shielding field is an expansion into a sum of Cartesian "box" harmonics, having the form

$$\exp\left(X\sqrt{\frac{1}{p^2}+\frac{1}{q^2}}\right)\cos\frac{Y}{P}\left\{\begin{array}{l}\sin(Z/q)\\ \cos(Z/q)\end{array}\right\}. \qquad (27)$$

The upper and lower factors in braces correspond to two types of symmetry: the terms with sin (Z/q) are for the untilted magnetosphere, while the terms with cos (Z/q) represent the perturbation field (their coefficients, to the lowest order, are proportional to the tilt angle Ψ). In fact, as was discussed in detail in T98, the extended form of the expansion with tilt-dependent perturbation terms is required only for the geodipole shielding field, while contributions of external sources, including those of the tail current, were treated in a simpler way, by deformations. In this approach we derived the confined tail field only for the case of zero tilt angle, $\Psi = 0$. The configurations for $\Psi \neq 0$ were then easily obtained by a global deformation of coordinates, defined by equations (7), (8), (9), (10), (11), (12), (13), and (14), which kept the field from all magnetospheric sources confined within the same tilt-dependent boundary. More details are provided in the following sections.

2.4.1. Shielding the dipole field within a tilt-dependent magnetopause

[63] As shown in T98, although applying the coordinate transformation (equations (11), (12), (13), and (14)) to the untilted shielded field of the Earth's dipole results in "visually reasonable" tilted configurations, there is a subtle problem, rooted in an intrinsic limitation of the deformation method. Namely, it leaves intact the mapping of the polar cusps, and hence the null points at the boundary map to the same latitude in the ionosphere for all dipole tilt angles, which disagrees with observations and model results. In addition, at close geocentric distances the deformation of an originally curl-free dipole field gives rise to relatively strong unphysical "stray" currents and to corresponding artificial contribution to $\mathbf{B}$, owing to the rapid increase of the dipolar field toward Earth. There is no simple way around that difficulty. However, because most of these inaccuracies arise from deformation of the dipole field, a compromise solution employed here was to use the deformation method for the other magnetic field sources but to use a different method to shield the tilted dipole field, using a tilt-dependent scalar potential composed of the harmonics (equation (27)).

[64] More specifically, we followed the method described in T98 (the appendix), in which the accuracy of the shielding was improved by rotating the potential fields (equation (27)) around the **Y** axis by an angle, proportional to the dipole tilt angle Ψ. In this particular realization of the approach the following forms were used:

$$\mathbf{B} = \hat{\mathbf{R}}_\perp^{-1}\sum_{i,\mathrm{k}=1}^{3}\mathbf{B}_{\perp ik}(\hat{\mathbf{R}}_\perp\mathbf{r}) + \hat{\mathbf{R}}_\|^{-1}\sum_{i,\mathrm{k}=1}^{3}\mathbf{B}_{\perp ik}(\hat{\mathbf{R}}_\|\mathbf{r}), \qquad (28)$$

where $\hat{\mathbf{R}}_\perp = \hat{\mathbf{R}}(\gamma_\perp)$ and $\hat{\mathbf{R}}_\| = \hat{\mathbf{R}}(\gamma_\|)$ are the matrices of rotation around the Y_{GSM} axis. The angles of the rotation, $\gamma_\perp$ and $\gamma_\|$, were defined by $\gamma_\perp = \kappa_\perp\ \Psi$ and $\gamma_\| = \kappa_\|\ \Psi$, and the coefficients $\kappa_\perp$ and $\kappa_\|$ were considered as free parameters and determined by minimizing the rms $\langle B_n^2\rangle$, together with other free parameters entering in equation (28).

[65] The fields $\mathbf{B}_{\perp ik}$ and $\mathbf{B}_{\| ik}$ in equation (28) were defined as

$$\mathbf{B}_{\perp ik} = -\nabla U_{\perp ik}, \quad \mathbf{B}_{\perp ik} = -\nabla U_{\| ik}, \qquad (29)$$

where

$$U_{\perp ik} = (a_{ik} + b_{ik}\cos\Psi)\exp\left(X\sqrt{\frac{1}{p_i^2}+\frac{1}{r_k^2}}\right)\cos\frac{Y}{p_i}\sin\frac{Z}{r_k} \qquad (30)$$

for i = 1, 2, 3 and k = 1, 2,

$$\begin{aligned}U_{\perp i3} = {} & (a_{i3} + b_{i3}\ \cos\Psi)\exp\left(X\sqrt{\frac{1}{p_i^2}+\frac{1}{r_3^2}}\right)\cos\frac{Y}{p_i}\\ & \cdot\left(Z\cos\frac{Z}{r^3} + \frac{X\sin\frac{Z}{r^3}}{r^3\sqrt{\frac{1}{p_i^2}+\frac{1}{r_3^2}}}\right)\end{aligned} \qquad (31)$$

for i = 1, 2, 3 and k = 3, and

$$U_{\| ik} = (c_{ik}\sin\Psi + d_{ik}\sin2\Psi)\exp\left(X\sqrt{\frac{1}{q_i^2}+\frac{1}{s_k^2}}\right)\cos\frac{Y}{q_i}\cos\frac{Z}{s_k} \qquad (32)$$

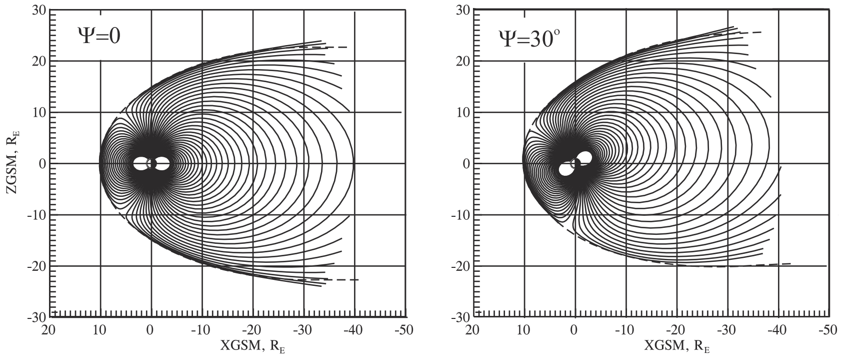

Figure 7. Shielded dipole fields, obtained using the scalar potentials (equation (34) and (35)), for (left) untilted dipole and (right) a tilted configuration with $\Psi = 30°$.

for $i = 1, 2, 3$ and $k = 1, 2, 3$. The potentials (equation (31)) were obtained by taking a derivative of equation (30) with respect to $1/r_k$; combining the potentials (equations (30) and (31)) was found necessary in order to avoid the tendency of the parameters r_k to cluster in close pairs, accompanied by an unlimited growth of the corresponding linear coefficients in the course of the iterative minimization of $\langle B_n^2 \rangle$. That problem has already been encountered in the construction of the T96 model and was discussed in an earlier paper [*Tsyganenko*, 1995, section 2.3]. The coefficients a_{ik}, b_{ik}, c_{ik}, d_{ik}, and the nonlinear parameters p_i, r_k, q_i, s_k, $\gamma_\perp$, and $\gamma_\|$, were fitted by least squares to minimize the rms residual $\langle B_n^2 \rangle$ over a set of points, distributed over the model magnetopause up to a tailward distance of 70 R_E. The set included four subsets, corresponding to four values of the dipole tilt angle in the range $0° < \Psi < 35°$ (negative tilts, resulting in redundant symmetric configurations, were not considered). The best fit solution was found to provide an rms residual B_n of 0.13 nT. Figure 7 shows a plot of the shielded dipole field line configuration and the shape of the model magnetopause.

2.4.2. Shielding of other external field sources

[66] The "box" harmonics (equation (27)) were also used to construct the shielding fields for all other magnetospheric current systems. In most cases the expansion coefficients also included a linear dependence on additional parameters, taking into account either the tilt-angle effects or a variable scale size of a current system, or both. A more detailed description for each source is given below.

2.4.2.1. Shielding of the tail field

[67] The tail shielding field was represented by two separate expansions of the "box" harmonics (equation (27)), corresponding to the "long" and "short" modules of the field of the cross-tail current, described in section 2.2.1. As already said, that allowed us to independently vary the amplitudes of the two modules, keeping the total tail field fully shielded within the magnetopause.

[68] As mentioned in section 2.2.2, the tilt-angle effects were taken into account by deforming together the tail field and its shielding field, which required deriving the shielding fields only for the untilted configuration. This saves much calculation, since there is no need to include in the expansion the terms of equation (27), containing $\cos(Z/q)$ (as was done in the T96 model).

[69] Another novelty here is an additional degree of freedom, namely, a variable shift of the cross-tail current along the X axis. In T96 the individual tail modules had fixed positions with respect to Earth, since any shift along the tail axis would require a recalculation of the shielding coefficients. In this model the problem was circumvented by including the shift ΔX as a linear parameter of the shielding field into each of the two tail field modules. More specifically, the expansion terms were chosen in the form

$$U_{ik} = (a_{ik} + b_{ik}\Delta X)\exp\left(X\sqrt{\frac{1}{p_i^2}+\frac{1}{r_k^2}}\right)\cos\frac{Y}{p_i}\sin\frac{Z}{r_k}, \qquad (33)$$

whose coefficients were determined by a standard least squares fitting routine but using an extended set of values of B_n on the model magnetopause, including those for different values of ΔX, distributed within the interval $-4 \le \Delta X \le 4$ R_E. Figure 8 shows two families of field lines for the shielded "long" module of the tail field, corresponding to $\Delta X = 4$ and $\Delta X = -4$. In both cases the fields are accurately confined within the model boundary, in spite of the large opposing shifts of the cross-tail current.

2.4.2.2. Shielding of the ring current

[70] The expansions for the shielding field potentials were derived separately for the symmetric and partial components of the ring current, in order to allow their parameters to vary independently in response to changing magnetospheric conditions. Mathematically, both were given the same form, similar to that for the geodipole (equations (28), (29), (30), (31), and (32)) but without the derivative term (equation (31)):

$$U_{\perp ik} = \left(a_{ik}^{(0)} + a_{ik}^{(1)}\Delta\xi + b_{ik}^{(0)}\cos\Psi + b_{ik}^{(1)}\Delta\xi\cos\Psi\right)\xi^3\exp \cdot\left(X\sqrt{\frac{1}{p_i^2}+\frac{1}{r_k^2}}\right)\cos\frac{Y}{p_i}\sin\frac{Z}{r_k}, \qquad (34)$$

$$U_{\| ik} = \left(c_{ik}^{(0)}\sin\Psi + c_{ik}^{(1)}\Delta\xi\sin\Psi + d_{ik}^{(0)}\sin 2\Psi + d_{ik}^{(1)}\Delta\xi\sin 2\Psi\right) \cdot\xi^3\exp\left(X\sqrt{\frac{1}{q_i^2}+\frac{1}{s_k^2}}\right)\cos\frac{Y}{q_i}\cos\frac{Z}{s_k}. \qquad (35)$$

Unlike the dipole shielding, the potentials (equations (34) and (35)) are multiplied by ξ^3, where ξ is the scaling factor quantifying the size of the ring current (section 2.1), which approximately compensates the overall change of its dipole

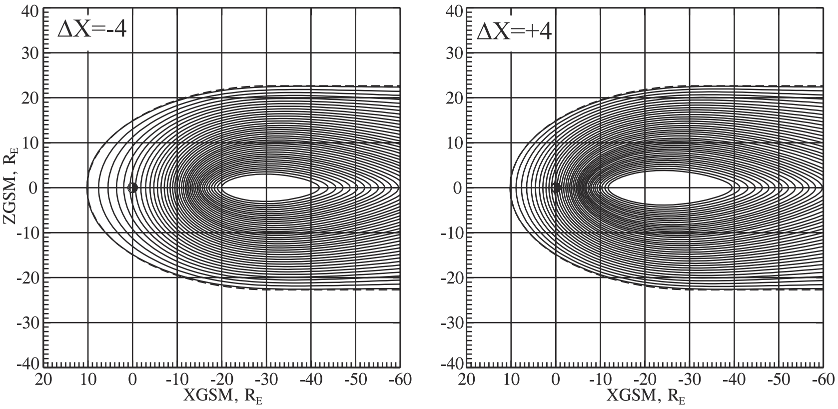

Figure 8. A family of the magnetic field lines of the "long" tail field module, including its shielding field, shifted tailward (left) and earthward (right) by $\Delta X = \pm 4\ R_E$.

moment. In addition, the coefficients also include a linear dependence on $\Delta\xi = \xi - 1$ (negative/positive values of $\Delta\xi$ signify a smaller/larger ring current). Figure 9 illustrates the performance of the potentials (equations (34) and (35)) by showing field lines of a tilted ring current (symmetric part), confined within the magnetopause.

[71] Note that the model partial ring current has one more nonlinear free parameter, in addition to the same set of coefficients and scaling factors as in the symmetric ring current, namely, its rotation angle δ with respect to the midnight meridian plane. In principle, the rotation of an axially asymmetric ring current affects the magnetopause shielding field, and hence that parameter should also be taken into account in the expansions (equations (34) and (35)). Since the rotation breaks the original symmetry of the magnetic field in the dawn-dusk direction, proper shielding of such a field would require adding to the potentials (equations (34) and (35)) another group of terms, antisymmetric with respect to *Y*. That would significantly increase the number of parameters and hence further complicate the model. As a compromise solution, we chose to ignore the effect of the PRC rotation in the shielding field. As can be seen from the following, the resulting inaccuracy is relatively small.

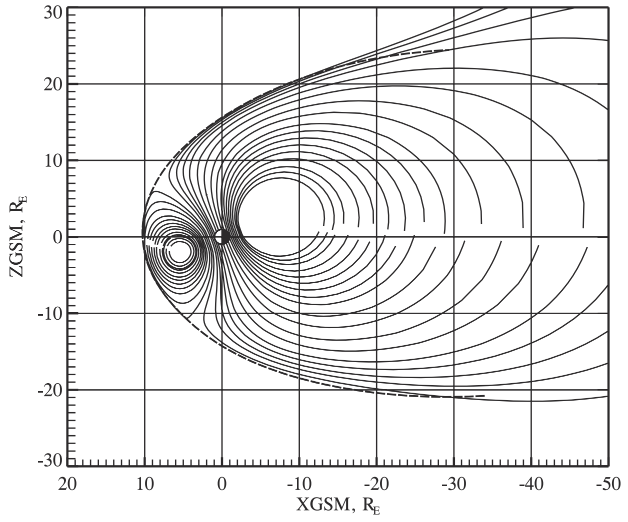

Figure 9. Field lines of the model ring current (axisymmetric part), shielded inside the model magnetopause. The ring current is coaxial with the Earth's dipole, tilted in this example by $\Psi = 20°$.

[72] The net field of the PRC can be represented by a sum of axially symmetric and quadrupole terms [*Tsyganenko*, 1993, 2000]. The axisymmetric term obviously does not contribute to the azimuthal field variation, which is therefore due solely to the quadrupole part, whose field decreases rapidly (as $\sim r^{-4}$) outside the PRC. As can be verified by calculating the contribution of the quadrupole term at different locations in the near magnetosphere [see *Tsyganenko*, 2000, Figure 14], a PRC with the total magnitude of 0.7 MA produces an asymmetry of ~20 nT between the opposite local time sectors in the inner magnetosphere, and the disturbance is almost entirely confined inside the PRC. In spite of the relatively large disturbance near Earth, it falls off to less than 1 nT at the magnetopause, so that the associated effect in the shielding field does not exceed a fraction of a nanotesla.

2.4.2.3. Shielding of the Region 1 and 2 Birkeland currents

[73] The Birkeland currents were shielded using expansions of the same scalar potentials as in equations (34) and (35) but without the common factor, similar to ξ^3. For the ring current that factor represented the first-order effect of its rescaling, related to a change of the magnetic moment, while the linear terms containing $\Delta\xi$ provided a second-order correction. That way of gauging the shielding field was possible owing to a relatively limited size of the ring current. In contrast, for the Birkeland currents it does not make sense to retain such a factor, since they extend over a larger spatial domain and have quite different geometry.

[74] As already noted in section 2.3.1, adding the shielding field is important, since it redirects the initially unbounded currents and makes them flow along the magnetopause, which is not only more correct conceptually but also brings the model field closer to the observed one. To visualize the geometry of the model Birkeland currents, a family of the current flow lines was plotted by calculating $\mathbf{j} = \nabla\times\ \mathbf{B}$ from the shielded model magnetic field, with all the sources except for the Region 1 field-aligned current

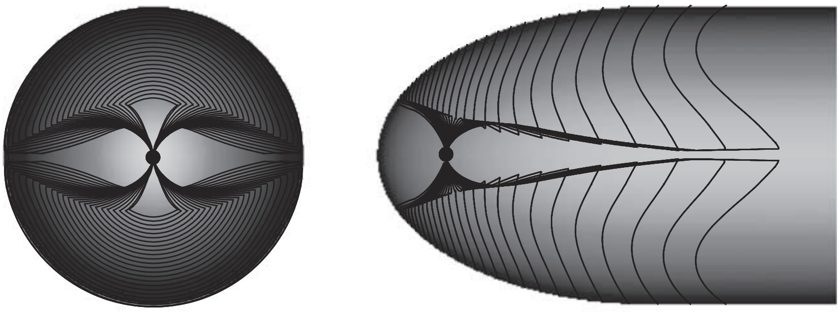

Figure 10. A family of the electric current flow lines, calculated as a curl of the magnetic field of the shielded Region 1 Birkeland current, illustrating their global geometry in the model: (left) front view (from Sun) and (right) side view (along the *Y* axis). Note that virtually all of the current closes via the high-latitude magnetopause upon reaching the boundary.

turned off. The result is shown in Figure 10. Note that the density of the lines was set arbitrarily and does not correspond to the actual current density; our purpose here was just to illustrate the global configuration of the model currents.

2.5. IMF-Related Interconnection Field

[75] Still in the early days of the space physics it was predicted that the existence of an IMF makes the magnetosphere open [*Dungey*, 1961]. The interconnection between the IMF and the geomagnetic field was introduced in several theoretical models, from a crude case of a uniform field added to a purely dipolar one [*Stern*, 1973], to quite sophisticated models [e.g., *Toffoletto and Hill*, 1989; 1993]. Our earlier work [*Tsyganenko*, 1996] attempted to derive the average interconnection field $\mathbf{B}_{\mathrm{INT}}$ from a large set of the magnetospheric *B* field measurements, combined with simultaneous IMF data. Inside the magnetosphere, $\mathbf{B}_{\mathrm{INT}}$ was a potential field, whose normal component across the magnetopause was controlled by the observed orientation and magnitude of the IMF in the upstream solar wind. The overall degree of the IMF penetration was quantified by a single coefficient, whose value was determined by fitting the entire model to data. In general, the magnitude of the penetrating field is relatively small as compared to the total field of magnetospheric sources; in addition, most of our data covered low and middle latitudes, while the interconnection effects should peak in the high-latitude magnetosphere, close to its boundary.

[76] Therefore, resolving the interconnection effect in the data-based model seemed like extracting a weak signal in the presence of appreciable noise. However, somewhat against expectation, fitting the model to the data yielded reasonable values of the penetration coefficient, between 0.15 and 0.80, even though that parameter was among the least accurate ones.

[77] The present model retains the interconnection term, even though it is focused on the inner magnetosphere. Aside from a few modifications, the initial approach was the same as in the T96 model, although the fitting results, presented in Paper 2, prompted us a much simpler solution, as detailed below.

[78] By definition, the penetrated interconnection field inside the magnetosphere is curl-free and hence can be uniquely defined as $\mathbf{B}_{\mathrm{INT}} = -\nabla U_{\mathrm{INT}}$, by specifying its normal component at the model magnetopause and then by solving a Neumann problem for the scalar potential U_{INT}. The normal component B_n was represented semiempirically, based on the following arguments. Assuming that the IMF ahead of the bow shock is known, and having in mind that the magnetic field in the magnetosheath is greatly modified by the bow shock and by its draping around the boundary, one can envision a priori two extreme cases: (1) a fully "opaque" magnetopause with $B_n = 0$ everywhere and (2) a "fully transparent" magnetopause, on which (ignoring for now the compression and draping) $B_n = \mathbf{B}^{\mathrm{IMF}} \cdot \mathbf{n}$, at any point with unit normal $\mathbf{n}$. Reality is probably somewhere between those extremes: the IMF is strongly compressed and deformed downstream from the bow shock, and the penetrating component B_n is smaller than that in the fully transparent approximation, though it is reasonable to assume it remains proportional to $\mathbf{B}^{\mathrm{IMF}} \cdot \mathbf{n}$, and the average orientation of the penetrated field inside the magnetosphere (in the sense of the clock angle) follows that of the IMF in the upstream solar wind. One can also expect that the extent of the IMF penetration at some point on the magnetopause depends on its tailward distance $X{-}X_s$ from the subsolar point. Furthemore, it can also depend on the point's distance Y', measured from the plane containing the X axis and rotated by the IMF clock angle θ from the noon-midnight meridian plane [*Toffoletto and Hill*, 1989].

[79] Based on the above arguments, the following approximation was at first adopted for the normal component at the magnetopause:

$$B_n = \left(\mathbf{B}_{\perp}^{\mathrm{IMF}} \cdot \mathbf{n}\right)\left[\mu_1 \exp\left(\frac{X - X_s}{\Delta X} - \frac{Y'^2}{\Delta Y'^2}\right) + \mu_2\right], \qquad (36)$$

where $\mathbf{B}_{\perp}^{\mathrm{IMF}}$ is the transverse component of the IMF, observed upstream from the bow shock (effects of the IMF B_x are ignored). The first term inside the square brackets empirically approximates the variation of B_n down the tail and away from the plane $Y' = 0$, with the *e*-folding distances ΔX and $\Delta Y'$, and the coefficient μ_1 quantifies the magnitude of that term. The coordinate Y' corresponds to a system, obtained from the standard GSM one by its rotation around the Sun-Earth line by the IMF clock angle, so that its Z' axis is aligned with $\mathbf{B}_\perp^{\mathrm{IMF}}$. The second term in the brackets, μ_2, corresponds to a uniform penetrating field. That term was absent in the T96 model, so that the penetrated magnetic field dropped down to zero in the distant tail, which resulted in abnormally small values of the mapped electric potentials across the polar cap (F. Toffoletto, private communication, 1997). In actuality, one expects B_n to asymptotically tend to a finite nonzero value in the distant tail, since the stationary merging with the IMF implies $\nabla \times \mathbf{E} = 0$ [*Toffoletto and Hill*, 1989].

[80] The normal component (equation (36)) was used for calculating parameters of an expansion for the magnetic scalar potential, representing the interconnection field inside the magnetosphere. As before, we used "box" harmonics, whose coefficients included a linear dependence on the parameters ΔX and ΔY:

$$U_{\mathrm{INT}} = \sum_{i,k=1}^{2} \left(a_{ik}^{(0)} + a_{ik}^{(1)} \Delta X + a_{ik}^{(2)} \Delta Y \right) \exp\left(X \sqrt{\frac{1}{p_i^2} + \frac{1}{r_k^2}} \right) \cdot \cos\frac{Y}{p_i} \sin\frac{Z}{r_k}. \tag{37}$$

The nonlinear parameters have also been expanded in the same way:

$$\begin{aligned} p_i &= p_i^{(0)} + p_i^{(1)} \Delta X + p_i^{(2)} \Delta Y, \\ r_k &= r_k^{(0)} + r_k^{(1)} \Delta X + r_k^{(2)} \Delta Y, \end{aligned} \tag{38}$$

and the values of $a_{ik}^{(l)}$, $p_i^{(l)}$, and $r_k^{(l)}$ were found by least squares fitting over the entire boundary of the normal field $\partial U_{\mathrm{INT}}/\partial n$, obtained from equations (37) and (38), to that given by equation (36) for a set of values of ΔX and ΔY within the intervals $10 \leq \Delta X \leq 25$ and $6 \leq \Delta Y \leq 24$. The obtained potential interconnection field (equations (37) and (38)) was included in the total model field, and the parameters μ_1, μ_2, ΔX, and ΔY were fitted by least squares to the observed field.

[81] Somewhat surprisingly, the parameters ΔX and ΔY were found to steadily increase in the course of iterations beyond the range of validity of the approximation (equations (37) and (38)), causing a steady decrease in the μ_1 term of equation (36). This suggested a nearly uniform penetration of the IMF inside the magnetosphere, so that eventually, instead of the complex interconnection field defined by the potential (equation (37)), we adopted a very simple one,

$$\mathbf{B}_{\mathrm{INT}} = \varepsilon \mathbf{B}_\perp^{\mathrm{IMF}}, \tag{39}$$

where the penetration coefficient ε was assumed to depend on the IMF clock angle θ, allowing for a possibility of different penetration efficiency during southward and northward IMF conditions. More details on the model parameterization and on results of its fitting to the data will be presented in Paper 2.

3. Summary

[82] A new magnetospheric magnetic field model has been developed, intended to replace the existing data-based T96 model [*Tsyganenko*, 1995, 1996]. To that end, advanced representations were introduced for all major sources of the field in the inner and near magnetosphere. The model ring current, originally derived from charged particle data, includes both axisymmetric and partial components, making it possible to represent strongly asymmetric disturbances during storm times. Another new element is a flexible global model of the contributions of large-scale Region 1 and 2 Birkeland currents, whose spatial extent and local time distribution can be easily varied and fitted to the spacecraft data. The model includes a revised approximation for the field of the cross-tail current sheet, comprising two modules with different rates of current density variation along the tail axis, a movable inner edge, variable thickness, and flexible shape, controlled by the tilt angle of the Earth's dipole. The model field of all magnetospheric sources is confined within a magnetopause, based on the recent approximation of *Shue et al.* [1998]. The size of the boundary is controlled by the solar wind pressure, and its shape varies in response to changes of the geodipole tilt angle. The model also includes a controlled interconnection with the IMF, making it possible to model open magnetospheric geometries.

[83] **Acknowledgments.** I am grateful to David Stern for his careful reading of the manuscript and numerous comments. I also would like to thank Arcadi Usmanov for providing some of his graphics codes and helpful advice on using them. Thanks are due to Frank Toffoletto for pointing out the problem with the mapping of electric potentials in the T96 model. This work is supported under NASA contract NAS5-32993 and NSF Magnetospheric Physics Program grant ATM-9819873.

[84] Janet G. Luhmann thanks Michael Schulz and another referee for their assistance in evaluating this paper.

References

Alexeev, I. I., E. S. Belenkaya, and C. R. Clauer Jr., A model of Region 1 field-aligned currents dependent on ionospheric conductivity and solar wind parameters, *J. Geophys. Res.*, *105*, 21,119, 1999.

Dungey, J. W., Interplanetary magnetic field and the auroral zones, *Phys. Rev. Lett.*, *6*, 47, 1961.

Erlandson, R. E., L. J. Zanetti, T. A. Potemra, P. F. Bythrow, and R. Lundin, IMF B_y dependence of Region 1 Birkeland currents near noon, *J. Geophys. Res.*, *93*, 9804, 1988.

Fok, M.-C., T. E. Moore, and M. E. Greenspan, Ring current development during storm main phase, *J. Geophys. Res.*, *101*, 15,311, 1996.

Fok, M.-C., T. E. Moore, and D. C. Delcourt, Modeling of inner plasma sheet and ring current during substorms, *J. Geophys. Res.*, *104*, 14,557, 1999.

Ganushkina, N. Y., T. I. Pulkkinen, and M. V. Kubyshkina, Modeling of ring current magnetic field during storms, in *Geophysical Research Abstracts* [CD-ROM], vol. 3, abstract 5937, Eur. Geophys. Soc., Katlenburg-Lindau, Germany, 2001.

Iijima, T., and T. A. Potemra, The amplitude distribution of field-aligned currents at northern high latitudes observed by Triad, *J. Geophys. Res.*, *81*, 5971, 1976.

Iijima, T., and T. A. Potemra, Large-scale characteristics of field-aligned currents associated with substorms, *J. Geophys. Res.*, *83*, 599, 1978.

Kozyra, J. U., V. K. Jordanova, J. E. Borovsky, M. F. Thomsen, D. J. Knipp, D. S. Evans, D. J. McComas, and T. E. Cayton, Effects of a high-density plasma sheet on ring current development during the November 2–6, 1993, magnetic storm, *J. Geophys. Res.*, *103*, 26,285, 1998.

Leontyev, S. V., and V. B. Lyatsky, Electric field and currents connected with *Y*-component of interplanetary magnetic field, *Planet. Space Sci.*, *22*, 811, 1974.

Liemohn, M. W., J. U. Kozyra, M. F. Thomsen, J. L. Roeder, G. Lu, J. E. Borovsky, and T. E. Cayton, Dominant role of the asymmetric ring current in producing the stormtime *Dst**, *J. Geophys. Res.*, *106*, 10,883, 2001.

Lui, A. T. Y., and D. C. Hamilton, Radial profiles of quiet time magnetospheric parameters, *J. Geophys. Res.*, *97*, 19,325, 1992.

Mead, G. D., and D. H. Fairfield, A quantitative magnetospheric model derived from spacecraft magnetometer data, *J. Geophys. Res.*, *80*, 523, 1975.

Newell, P., and C.-I. Meng, Dipole tilt effects on the latitude of the cusp and cleft/low-latitude boundary layer, *J. Geophys. Res.*, *94*, 6949, 1989.

Petrinec, S. M., and C. T. Russell, An empirical model of the size and shape of the near-Earth magnetotail, *Geophys. Res. Lett.*, *20*, 2695, 1993.

Roelof, E. C., and D. G. Sibeck, Magnetopause shape as a bivariate function of the interplanetary magnetic field B_z and solar wind dynamic pressure, *J. Geophys. Res.*, *98*, 21,421, 1993.

Schulz, M., and M. McNab, Source-surface model of the magnetosphere, *Geophys. Res. Lett.*, *14*, 182, 1987.

Shue, J.-H., P. Song, C. T. Russell, J. T. Steinberg, J. K. Chao, G. Zastenker, O. L. Vaisberg, S. Kokubun, H. J. Singer, T. R. Detman, and H. Kawano, Magnetopause location under extreme solar wind conditions, *J. Geophys. Res.*, *103*, 17691, 1998.

Sibeck, D. G., R. E. Lopez, and E. C. Roelof, Solar wind control of the magnetopause shape, location and motion, *J. Geophys. Res*, *96*, 5489, 1991.

Stern, D. P., Tail modeling in a stretched magnetosphere, 1, Methods and transformations, *J. Geophys. Res.*, *92*, 4437, 1987.

Stern, D. P., A study of the electric field in an open magnetosphere, *J. Geophys. Res.*, *78*, 7292, 1973.

Stern, D. P., The art of mapping the magnetosphere, *J. Geophys. Res.*, *99*, 17,169, 1994.

Toffoletto, F. R., and T. W. Hill, Mapping of the solar wind electric field to the Earth's polar caps, *J. Geophys. Res.*, *94*, 329, 1989.

Toffoletto, F. R., and T. W. Hill, A nonsingular model of the open magnetosphere, *J. Geophys. Res.*, *98*, 1339, 1993.

Tsyganenko, N. A., Global quantitative models of the geomagnetic field in the cislunar magnetosphere for different disturbance levels, *Planet. Space Sci.*, *35*, 1347, 1987.

Tsyganenko, N. A., A magnetospheric magnetic field model with a warped tail current sheet, *Planet. Space Sci.*, *37*, 5, 1989.

Tsyganenko, N. A., Quantitative models of the magnetospheric magnetic field: Methods and results, *Space Sci. Rev.*, *54*, 75, 1990.

Tsyganenko, N. A., Methods for quantitative modeling of the magnetic field from Birkeland currents, *Planet. Space Sci.*, *39*, 641, 1991.

Tsyganenko, N. A., A global analytical representation of the magnetic field produced by the Region 2 Birkeland currents and the partial ring current, *J. geophys. Res.*, *98*, 5677, 1993.

Tsyganenko, N. A., Modeling the Earth's magnetospheric magnetic field confined within a realistic magnetopause, *J. geophys. Res.*, *100*, 5599, 1995.

Tsyganenko, N. A., Effects of the solar wind conditions on the global magnetospheric configuration as deduced from data-based field models, *Eur. Space Agency Spec. Publ., ESA SP-389*, *181*, 1996.

Tsyganenko, N. A., Modeling of twisted/warped magnetospheric configurations using the general deformation method, *J. Geophys. Res.*, *103*, 23,551, 1998.

Tsyganenko, N. A., Modeling the inner magnetosphere: The asymmetric ring current and Region 2 Birkeland currents revisited, *J. Geophys. Res.*, *105*, 27,739, 2000.

Tsyganenko, N. A., Empirical magnetic field models for the space weather program, *in Space Weather, Geophys. Monogr. Ser.*, vol. 125, edited by P. Song, H. Singer, and G. L. Siscoe, p. 273, AGU, Washington, D.C., 2001.

Tsyganenko, N. A., A model of the near magnetosphere with a dawn-dusk asymmetry, 2, Parameterization and fitting to observations, *J. Geophys. Res.*, 10.1029/2001JA000220, in press, 2002.

Tsyganenko, N. A., and M. Peredo, Analytical models of the magnetic field of disk-shaped current sheets, *J. Geophys. Res.*, *99*, 199, 1994.

Tsyganenko, N. A., and D. P. Stern, Modeling the global magnetic field of the large-scale Birkeland current systems, *101*, *27*, 187, 1996.

Tsyganenko, N. A., and A. V. Usmanov, Determination of the magnetospheric current system parameters and development of experimental geomagnetic field models based on data from IMP and HEOS, satellites, *Planet. Space Sci.*, *30*, 985, 1982.

Tsyganenko, N. A., S. B. P. Karlsson, S. Kokubun, T. Yamamoto, A. J. Lazarus, K. W. Ogilvie, and C. T. Russell, Global configuration of the magnetotail current sheet as derived from Geotail, Wind, IMP 8 and ISEE 1/2 data, *J. geophys. Res*, *103*, 6827, 1998.

Zhou, X.-W., C. T. Russell, and G. Le, Local time and interplanetary magnetic field *By* dependence of field-aligned currents at high altitudes, *J. Geophys. Res.*, *105*, 2533, 2000.

N. A. Tsyganenko, USRA, Code 690.2, Laboratory for Extraterrestrial Physics, NASA Goddard Space Flight Center, Greenbelt, MD 20771, USA. (kolya@nssdca.gsfc.nasa.gov)